AGU PUBLICATIONS

Geophysical Research Letters

RESEARCH LETTER
10.1002/2015GL063827

Key Points:
- Salinity anomalies on density surfaces are used to investigate eddy stirring
- Mixing length and horizontal diffusivity are estimated in the upper 2000 m
- Horizontal diffusivity varies by more than two orders of magnitude

Correspondence to:
S. T. Cole,
scole@whoi.edu

Citation:
Cole, S. T., C. Wortham, E. Kunze, and W. B. Owens (2015), Eddy stirring and horizontal diffusivity from Argo float observations: Geographic and depth variability, *Geophys. Res. Lett.*, *42*, 3989–3997, doi:10.1002/2015GL063827.

Received 11 MAR 2015
Accepted 24 APR 2015
Accepted article online 29 APR 2015
Published online 21 MAY 2015

Eddy stirring and horizontal diffusivity from Argo float observations: Geographic and depth variability

Sylvia T. Cole[1], Cimarron Wortham[2], Eric Kunze[3], and W. Brechner Owens[1]

[1]Woods Hole Oceanographic Institution, Woods Hole, Massachusetts, USA, [2]Applied Physics Laboratory, University of Washington, Seattle, Washington, USA, [3]Northwest Research Associates, Redmond, Washington, USA

Abstract Stirring along isopycnals is a significant factor in determining the distribution of tracers within the ocean. Salinity anomalies on density surfaces from Argo float profiles are used to investigate horizontal stirring and estimate eddy mixing lengths. Eddy mixing length and velocity fluctuations from the ECCO2 global state estimate are used to estimate horizontal diffusivity at a 300 km scale in the upper 2000 m with near-global coverage. Diffusivity varies by over two orders of magnitude with latitude, longitude, and depth. In all basins, diffusivity is elevated in zonal bands corresponding to strong current regions, including western boundary current extension regions, the Antarctic Circumpolar Current, and equatorial current systems. The estimated mixing lengths and diffusivities provide an observationally based data set that can be used to test and constrain predictions and parameterizations of eddy stirring.

1. Introduction

Eddies of all sizes continually stir oceanic tracers such as heat, salt, oxygen, and nutrients along isopycnal surfaces. This stirring impacts basin-scale tracer distributions and influences physical and biological systems. Along-isopycnal stirring is parameterized in numerical models as a horizontal diffusivity κ_h that represents processes on unresolved horizontal scales [e.g., *Fox-Kemper et al.*, 2013]. Numerical studies have shown that the large-scale ocean circulation and Earth's climate are sensitive to the magnitude and spatial distribution of parameterized horizontal eddy diffusivity [*Danabasoglu and McWilliams*, 1995; *Danabasoglu and Marshall*, 2007; *Eden et al.*, 2009; *Liu et al.*, 2012; *Fox-Kemper et al.*, 2013]. Since non-eddy-resolving ocean models currently use a variety of spatially varying diffusivity parameterizations, a better understanding of how and why stirring and diffusivity vary spatially is needed.

Several approaches have been used to investigate horizontal diffusivity. Challenges include capturing (i) the full range of horizontal scales at which eddy stirring takes place, and (ii) geographic and depth variability. Estimates based on tracer-release experiments [*Ledwell et al.*, 1998; *Tulloch et al.*, 2014] and isopycnal-following floats [*Zhang et al.*, 2001; *LaCasce et al.*, 2014] are limited in geographic extent and density range. Estimates based on natural tracer fluctuations are also geographically limited due to the large number of observations required to quantify tracer variance [*Armi and Stommel*, 1983; *Jenkins*, 1987; *Ferrari and Polzin*, 2005; *Cole et al.*, 2010; *Naveira Garabato et al.*, 2011; *Cole and Rudnick*, 2012]. Global estimates of horizontal diffusivity have been derived from (i) surface drifter tracks that are limited by the sparseness of the drifter distribution [*Zhurbas and Oh*, 2003, 2004; *Klocker et al.*, 2012a, 2012b; *Zhurbas et al.*, 2014] and (ii) satellite-derived estimates that do not resolve all scales of eddy activity [*Stammer*, 1998; *Waugh and Abraham*, 2008; *Abernathey and Marshall*, 2013], with neither capturing stirring below the surface. Efforts to infer the full three-dimensional field of horizontal diffusivity rely on numerical and theoretical models [*Ferreira et al.*, 2005; *Menemenlis et al.*, 2005; *Griesel et al.*, 2010; *Zika et al.*, 2010; *Liu et al.*, 2012; *Vollmer and Eden*, 2013; *Bates et al.*, 2014; *Chen et al.*, 2014], or observations in geographically limited areas [e.g., *Funk et al.*, 2009]. Such studies have found that horizontal diffusivities vary with location and depth, ranging from near zero to order $10^4\ m^2\ s^{-1}$. Basin-scale to global-scale observationally based data sets are not currently available to test predictions or parameterizations of eddy stirring.

This analysis provides a near-global estimate of horizontal diffusivity in the upper 2000 m. It is only recently through the Argo program [*Roemmich et al.*, 2009] that enough observations of a tracer, in this case salinity on density surfaces, have become available on a global scale to investigate eddy stirring. Argo observations are

typically used to investigate meso- and larger-scale phenomena [e.g., *Johnson et al.*, 2012] but do contain tracer fluctuations from all horizontal scales at which eddy stirring occurs. Horizontal diffusivity is a function of length scale [*Richardson*, 1926; *Okubo*, 1971] and here is estimated at a 300 km scale, which is similar to the scale of the largest quasigeostrophic eddies and larger than the Rossby deformation radius [*Chelton et al.*, 1998; *Chelton et al.*, 2011]. Diffusivity is estimated using a mixing-length framework [*Taylor*, 1915; *Prandtl*, 1925; *Tennekes and Lumley*, 1972] that combines tracer fluctuations from Argo observations with velocity fluctuations from the ECCO2 state estimate. The Argo float observations and ECCO2 velocity field are described in section 2, with methods for estimating mixing length and horizontal diffusivity presented in section 3. Results (section 4) and conclusions (section 5) follow.

2. Data

This analysis uses Argo float observations (obtained from ARGO GDAC, doi: 10.12770/1282383d-9b35-4eaa-a9d6-4b0c24c0cfc9) over the period 2005–2012. Approximately 3000 Argo floats, distributed throughout the ice-free ocean, return profiles of temperature, salinity, and pressure about once every 10 days from the surface to between 1000 and 2000 dbar [*Roemmich et al.*, 2009]. Most floats have a vertical resolution that ranges from 10 m near the surface to 100 m at depth; 10% of floats have a constant 2 m vertical resolution. Only delayed-mode data with quality control flags of 1 (indicating "good data" passing Argo quality control and statistical tests) are included. Gaps in pressure greater than 250 m are excluded from the analysis, affecting portions of less than 1% of profiles. In total, 705,795 profiles are used with more than 50% extending below 1500 dbar. Mapped larger-scale temperature and salinity fields on pressure surfaces derived solely from Argo observations are also used [*Roemmich and Gilson*, 2009]. Mapped fields are available for each month and year of Argo float observations on a $1° \times 1°$ grid.

Velocity fluctuations on a global scale at all depths are best obtained from ocean state estimates that assimilate data, and the ECCO2 product [*Menemenlis et al.*, 2005, 2008] is used here. The ECCO2 product uses a Green's function method [*Menemenlis et al.*, 2005] to adjust a small number of control parameters to produce a dynamically consistent run of the MITgcm [*Marshall et al.*, 1997] constrained to observations. Control parameters include initial and boundary conditions, drag coefficients, ice/ocean/snow albedo, viscosity, and diffusivity. Observational constraints include time-mean sea level, sea level anomaly, sea surface temperature, temperature, and salinity profiles from WOCE, TAO, Argo, XBT, and other available sources. ECCO2 is run on a cube-sphere grid with a mean horizontal spacing of 18 km and 50 vertical levels (the name for this run is cube92). Archived model output of 1 month averaged velocity fields interpolated to a regular ¼° latitude-longitude grid over 2005–2012 is used. When compared with moored current-meter observations, ECCO2 eddy kinetic energy (EKE) captured about 80% of observed EKE in high-EKE regions and about 50% in low-EKE regions [*Wortham*, 2013].

3. Methods

A mixing-length framework that relates observed tracer anomalies to gradients of the mean tracer field is used to estimate horizontal diffusivity. A convenient tracer is the salinity anomalies S' on isopycnal surfaces (which is proportional to the spice anomaly $2\beta S' = 2\alpha\theta'$ where α and β are the thermal expansion and saline contraction coefficients [*Veronis*, 1972; *Munk*, 1981]). Mixing length λ and horizontal diffusivity κ_h are estimated as follows:

$$\lambda = \langle S'S' \rangle^{\frac{1}{2}} / \langle \, | \nabla \{S\} | \, \rangle \tag{1a}$$

$$\kappa_h = c_0 \lambda u_{rms} \tag{1b}$$

where $S' = S - \{S\}$ is the salinity anomaly on a density surface, $u_{rms} = \langle (u - \{u\})^2 + (v - \{v\})^2 \rangle^{1/2}$ a characteristic velocity scale of the eddy field, c_0 a mixing efficiency, braces $\{\,\}$ indicate a 1 year running average within a grid box, and brackets $\langle\,\rangle$ a temporal average over all years [*Tennekes and Lumley*, 1972; *Armi and Stommel*, 1983; *Naveira Garabato et al.*, 2011]. The choice of a 1 year timescale is discussed below. Mixing length represents the distance a fluid parcel is transported before significant irreversible mixing occurs, and equation (1a) is valid when the background gradient varies slowly. Only 4% of mixing lengths estimated using equation (1a) are unrealistically large due to small mean gradient $\langle \, | \nabla \{S\} | \, \rangle$ (see below). Mixing length and diffusivity estimates using equation (1) are directed perpendicular to the mean salinity field (across salinity fronts), so

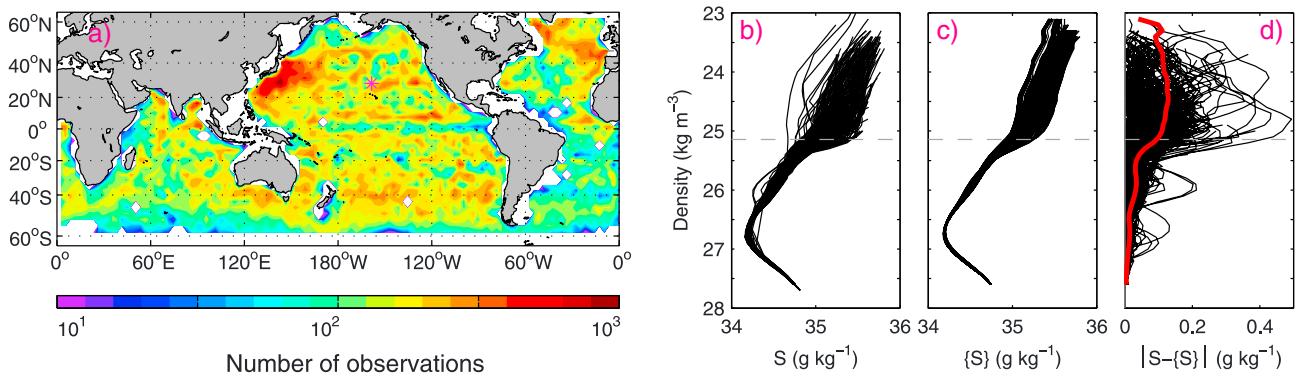

Figure 1. (a) Number of observations per 3° × 3° bin at 500 m depth. Magenta star (28.5°N, 159.5°W) indicates the grid box shown in Figures 1b–1d. Profiles as a function of density in one grid box of (b) salinity, S, (c) mean salinity, $\{S\}$, associated with each profile, and (d) magnitude of salinity fluctuations, $|S'| = |S - \{S\}|$, with $\langle S'S' \rangle^{1/2}$ shown in red. Mean salinity is the monthly profile of *Roemmich and Gilson* [2009] smoothed with a 1 year running average and interpolated in space and time to match each Argo profile. The dashed gray line indicates the density of the winter mixed-layer base, defined as the density corresponding to the shallowest depth below the mixed layer observed by at least 80% of the profiles in the grid box.

no information is obtained about stirring along isohalines (along salinity fronts). Estimated diffusivity and gradients in the mean salinity field are typically directed across mean streamlines (that is meridional in the interior or perpendicular to major frontal systems such as the Gulf Stream).

Salinity anomalies are considered in 3° × 3° spatial bins and defined with respect to a mean salinity field that has a 1 year timescale. Three-degree spatial bins are chosen to be comparable to the scale of the dominant eddies and correspond to tens to hundreds of profiles per grid box (Figure 1a). Salinity anomalies S' (Figure 1d) associated with each salinity profile S (Figure 1b) are determined by first excluding the mixed layer (since mixed-layer salinity anomalies are not expected to obey equation (1) due to surface forcing) and then removing a mean salinity $\{S\}$ on each density surface (Figure 1c). The mixed layer is excluded using the *Holte and Talley* [2009] mixed-layer-depth algorithm based on density, or a density threshold of 0.03 kg m^{-3} when this algorithm fails (0.6% of profiles). Mean salinity profiles $\{S\}$ (Figure 1c) are constructed by smoothing the *Roemmich and Gilson* [2009] monthly mapped salinity field with a 1 year running average, then interpolating in space and time to the location and time of each Argo profile. Removing a mean that varies slowly in time takes into account interannual variability and large-scale meandering of major fronts. Seasonal variability is not explicitly excluded. Estimated mixing lengths and the results of this analysis are not significantly different if salinity anomalies are restricted to timescales shorter than 1 month; seasonal variations on density surfaces do not significantly contribute to salinity anomalies, consistent with prior observations even near the base of the winter mixed layer [e.g., *Cole and Rudnick*, 2012]. In each grid box, density surfaces with less than 25 estimates of S' are excluded. Salinity anomalies so defined (Figure 1d) represent scales less than 300 km and 1 year, which include the dominant scales associated with mesoscale (and smaller-scale) eddies. The Argo-based salinity anomalies shown in Figure 1 (28.5°N, 159.5°W) agree well with those anomalies observed in this location using autonomous gliders [*Cole and Rudnick*, 2012]; both data sets reveal local maxima in the standard deviation of salinity near $\sigma_\theta = 25.0$ and 26.0 kg m^{-3}. The standard deviation of Argo-based salinity anomalies captures the persistent spatial patterns of mesoscale and smaller-scale salinity fluctuations.

Mixing length, equation (1a), is estimated using the salinity anomalies defined above and the mean salinity $\{S\}$ derived from *Roemmich and Gilson* [2009]. The salinity gradient for each year of observations is estimated as the average magnitude of the 3° forward and backward spatial differences (e.g., $|\nabla_x\{S\}| = \frac{1}{2}|\nabla_{x+}\{S\}| + \frac{1}{2}|\nabla_{x-}\{S\}|$). This is formally equivalent to a 6° centered difference for a planar salinity surface but does not underestimate the salinity gradient for symmetric salinity surfaces (for which a centered difference would result in zero gradient and an ill-conditioned mixing length). The salinity gradient is then averaged over all years. Near coastlines, forward or backward gradients are extrapolated using the nearest neighbor. Mixing lengths are considered valid if they are less than the horizontal scale at which the salinity gradient is calculated since a separation of scale between the eddy and mean fields is assumed in equation (1). Only 4% of mixing lengths, primarily along deeper density

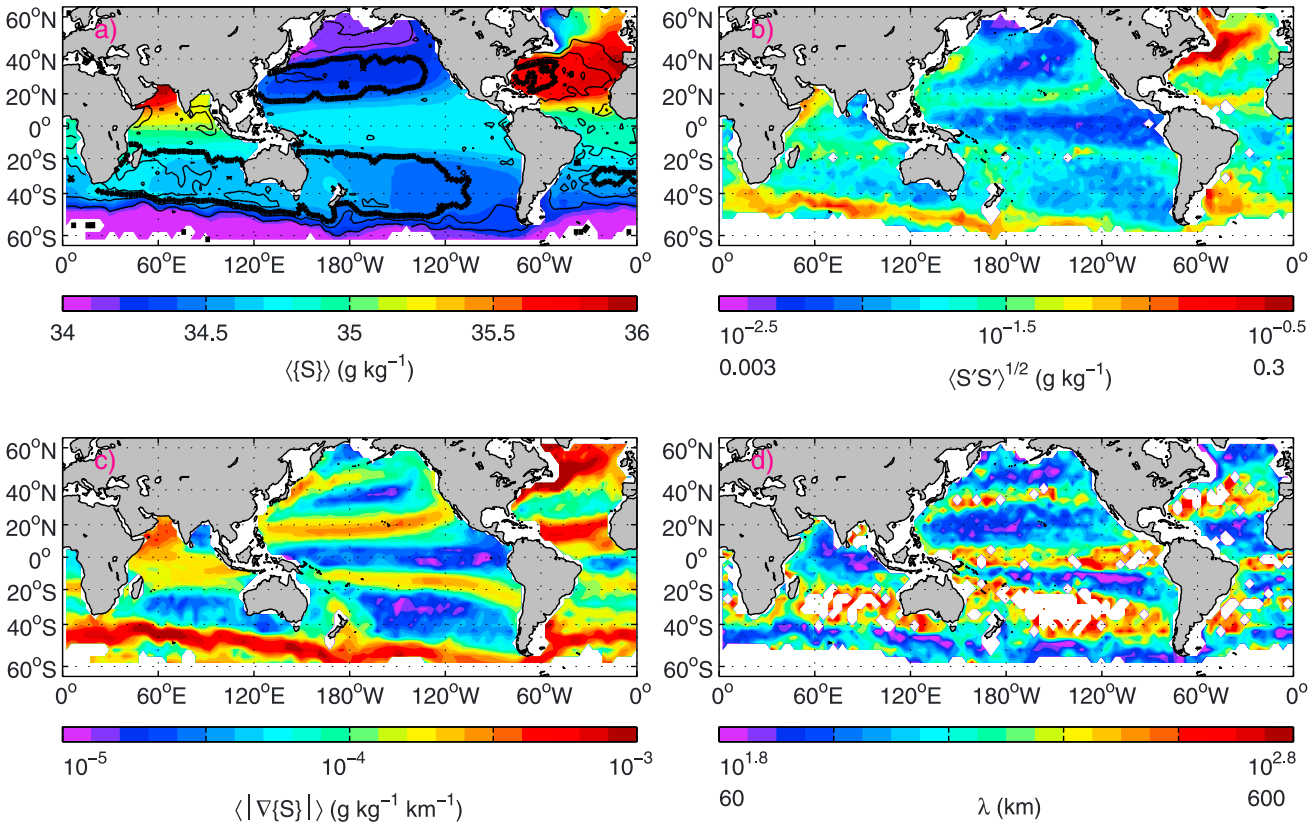

Figure 2. Statistics on the 27.0 kg m^{-3} density surface in 3° × 3° latitude bins of (a) mean salinity with depth contours in 200 m intervals and the 600 m surface in bold, (b) salinity standard deviation, (c) horizontal gradient of mean salinity, and (d) mixing length. Data gaps in Figure 2b correspond to grid boxes with less than 25 observations and in Figure 2d correspond to inferred mixing lengths greater than 600 km.

surfaces where the salinity gradient is weak, exceed 600 km and are excluded from analysis. Mixing lengths are interpolated to depth surfaces using the mean density-depth relation in each grid box.

Horizontal diffusivity, equation (1b), is estimated using a constant mixing efficiency (c_0) and velocity fluctuations (u_{rms}) from the ECCO2 state estimate. A constant mixing efficiency of 0.16 is used [*Wunsch*, 1999; *Klocker and Abernathey*, 2014, Appendix B], which in part accounts for salinity and velocity anomalies generated by meandering or reversible motions that do not result in stirring. The characteristic eddy speed u_{rms} is calculated on the ¼° ECCO2 grid, then bin-averaged to the 3° grid of this analysis. Velocity fluctuations represent scales from 1 month to 1 year that include the dominant mesoscale eddy motions, similar to salinity anomalies.

A sample calculation is shown for the 27.0 kg m^{-3} isopycnal (Figure 2), which ranges in depth from near 800 m in the subtropics to outcropping at the highest latitudes (Figure 2a). Mean salinity reflects the circulation at this depth, with distinct salinity values associated with subtropical gyres and equatorial regions (Figure 2a). The standard deviation of salinity anomalies (Figure 2b), as well as the horizontal gradient of the mean salinity field (Figure 2c), is elevated where different water masses meet, such as at the boundaries of the subtropical gyres. In each ocean, salinity anomalies are well correlated in space with horizontal gradients of the mean salinity field ($r^2 = 0.8$–0.9 depending on density; scatter is associated with geographic variations in mixing length) and only moderately correlated with vertical gradients of the mean salinity field ($r^2 = 0.4$–0.6). This indicates that horizontal stirring is more influential than vertical mixing in determining salinity anomalies on these scales, and a mixing length approach is appropriate. Mixing lengths vary from 10 km to the upper bound of 600 km (Figure 2d) with elevated values in zonal bands.

4. Results

A near-surface estimate of horizontal diffusivity is constructed that represents the diffusivity at the base of the winter mixed layer (Figure 3). The winter mixed-layer base (Figure 3a) is defined for each 3° × 3° grid

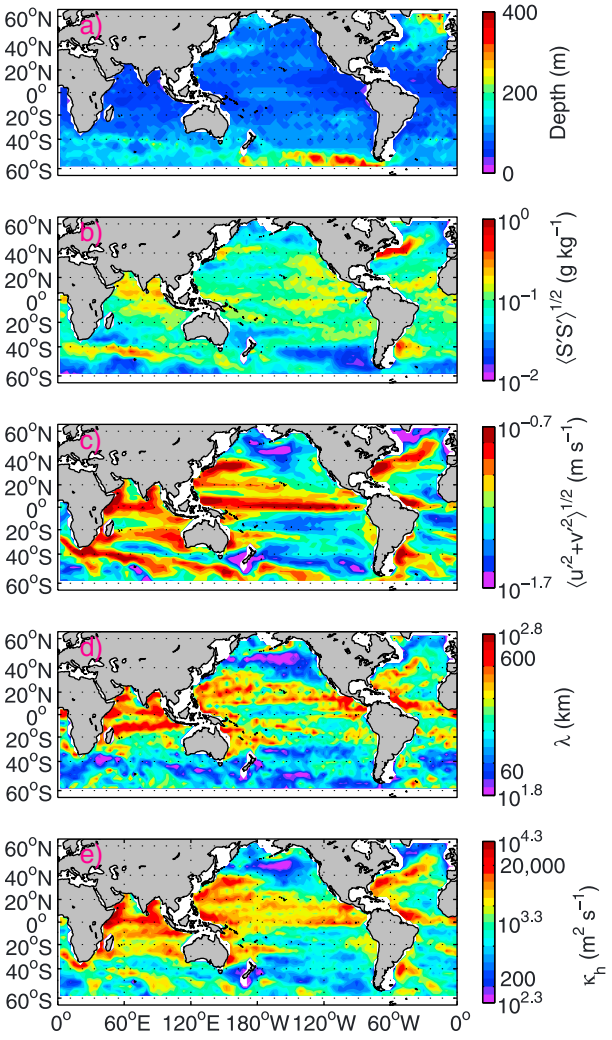

Figure 3. Estimates at the base of the winter mixed layer of (a) depth, (b) salinity standard deviation, (c) ECCO2 velocity standard deviation, (d) mixing length, and (e) horizontal diffusivity. The base of the winter mixed layer is defined as the shallowest depth below the mixed layer observed by at least 80% of the profiles in that grid box.

box as the shallowest depth identified as below the mixed layer in at least 80% of the profiles in that grid box. Salinity anomalies and mixing lengths are elevated in zonal bands (Figures 3b and 3d), similar to the spatial pattern observed along density surfaces (e.g., Figure 2). ECCO2 velocity fluctuations are also elevated in zonal bands corresponding primarily to western boundary current extension regions, equatorial currents, and the Antarctic Circumpolar Current (Figure 3c). Geographic variations in both mixing length and velocity fluctuations contribute to geographic variations in diffusivity. Since horizontal diffusivity varies by two orders of magnitude from 10^2 to 10^4 m^2 s^{-1} (Figure 3e), even factor-of-two uncertainties in ECCO2 velocity fluctuations are tolerable. The magnitude and geographic variation of horizontal diffusivity are qualitatively consistent with surface estimates based on satellite altimetry [*Abernathey and Marshall*, 2013; *Klocker and Abernathey*, 2014] and the maximum diffusivity estimated from surface drifters [*Zhurbas et al.*, 2014].

The magnitude of salinity anomalies, velocity fluctuations, mixing length, and horizontal diffusivity are shown as zonal averages in each ocean basin (Figure 4), which is appropriate given the zonal nature of these fields (Figures 2, 3). The magnitude of salinity anomalies (Figures 4a–4c) generally decreases with depth in each ocean basin, which reflects enhanced large-scale mean salinity gradients near the surface. At depth, patches of elevated salinity anomalies result from stirring of locally elevated mean salinity gradients (e.g., the elevated mean salinity gradient and magnitude of the salinity anomalies near 45°N in the Atlantic).

Mixing lengths (Figures 4g–4i) and horizontal diffusivities (Figures 4j–4l) are elevated (i) near the surface at tropical and subtropical latitudes, and (ii) at depth in strong current regions. Mixing lengths have both surface and subsurface maxima. Diffusivity has less pronounced subsurface maxima due to the decay with depth of the velocity field (Figures 4d–4f). Spatial patterns in mixing length and horizontal diffusivity are qualitatively consistent with recent theoretical arguments: elevated values occur at depth near regions with strong currents and enhanced velocity fluctuations such as western boundary current extension regions near ±40–50° in each ocean (Figures 4d–4f). Such regions also coincide with potential vorticity gradients that are near zero [*Tulloch et al.*, 2011, Figure 2]. These theories [*Ferrari and Nikurashin*, 2010; *Bates et al.*, 2014] suggest that such spatial variations result from the suppression of mixing length and horizontal diffusivity when eddies propagate at speeds different from the mean flow speed. Values are maximized when eddy phase speeds and mean flow speeds are similar, which occurs at depth in western boundary current regions and the Antarctic Circumpolar Current [*Tulloch et al.*, 2014; *Bates et al.*, 2014;

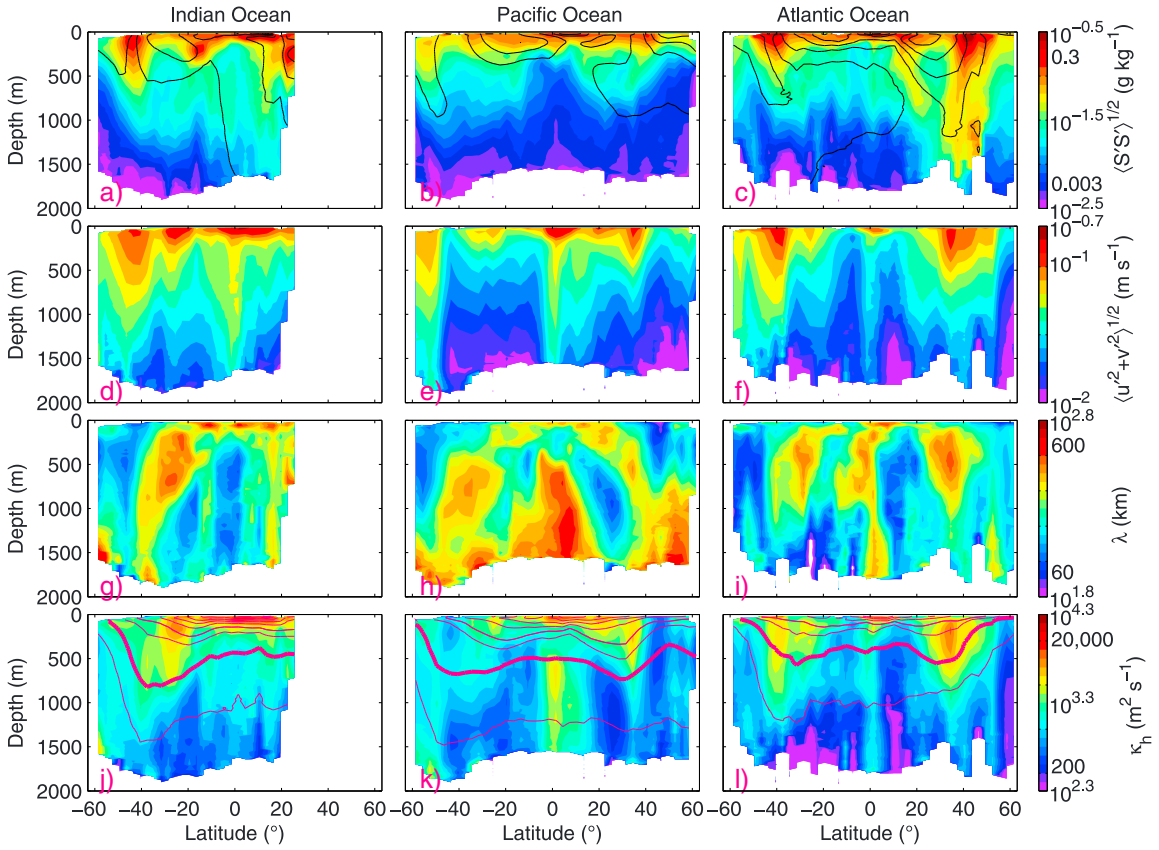

Figure 4. Zonally averaged (a–c) salinity standard deviation with average salinity (black contours), (d–f) ECCO2 velocity fluctuations, (g–i) mixing length, and (j–l) horizontal diffusivity with average density (magenta contours; 27.0 kg m^{-3} in bold) in the (a, d, g, and j) Indian Ocean, (b, e, h, and k) Pacific Ocean, and (c, f, i, and l) Atlantic Ocean.

Chen et al., 2014]. A more detailed comparison with this theoretical framework will be addressed in a future study. Globally averaged horizontal diffusivity is 1800 m^2 s^{-1} in the upper 1000 m (1600 m^2 s^{-1} in the upper 2000 m), around a factor of two larger than values typically used in numerical models likely due to excluding values at deeper depths and higher latitudes. The spatial pattern of diffusivity is likely more robust than its magnitude.

The complex current systems in equatorial regions lead to elevated mixing lengths and diffusivities at all depths. In all basins, diffusivity below 500 m depth within approximately 10° of the equator is elevated above subtropical values at similar depths. The large horizontal, vertical, and temporal variations in velocity caused by features such as equatorial undercurrents, equatorial countercurrents, equatorial deep jets, Kelvin waves, and tropical instability waves likely give rise to this increased equatorial diffusivity, although the mechanisms are presently not clear. Below 500 m depth near the equator, the Atlantic Ocean has the smallest diffusivities (700 m^2 s^{-1}) and the Pacific Ocean the largest (1900 m^2 s^{-1}; Figures 4g–4l). Studies in the Atlantic Ocean of equatorial deep jets [*Greatbatch et al.*, 2012] and oxygen structure [*Brandt et al.*, 2008] have found that a horizontal diffusivity of 300–400 m^2 s^{-1} explains observed features, smaller than our estimate of 700 m^2 s^{-1}. Estimates at depth in the Pacific and Indian Ocean are lacking. Verification of the depth structure of diffusivity and its variations between ocean basins along the equator is desirable from other studies, especially given the small salinity gradients and salinity anomalies in the equatorial Pacific Ocean.

To further characterize how diffusivities vary with depth, the prevalence of subsurface maxima and large changes with depth are considered. In 27% of the grid boxes, the maximum value of κ_h was more than 100 m below the base of the winter mixed layer (Figure 5a). Such subsurface maxima are primarily found at higher latitudes with the deepest subsurface maxima in the Antarctic Circumpolar Current region. The

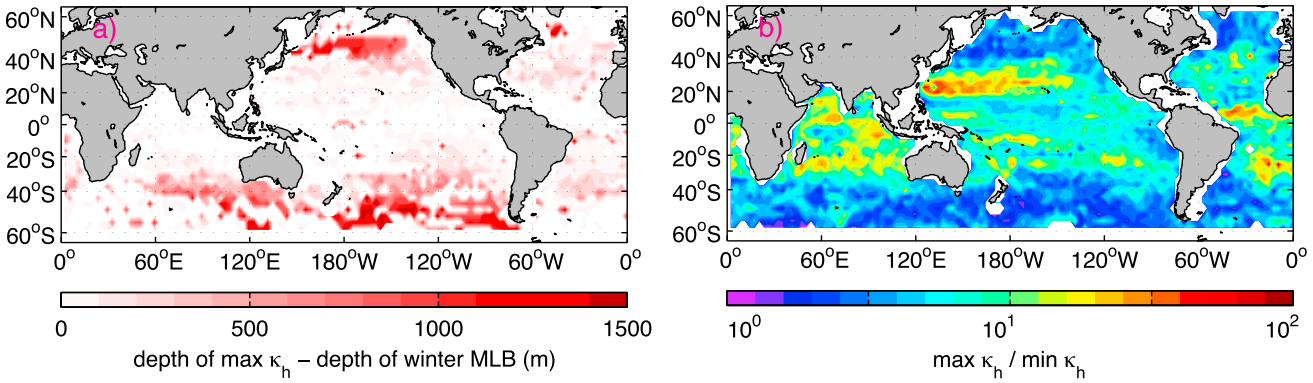

Figure 5. Statistics of κ_h in each grid box. (a) Depth of the maximum κ_h below the base of the winter mixed layer. (b) Ratio of maximum to minimum κ_h.

ratio of maximum to minimum κ_h in each grid box is a simple estimate of how much diffusivities vary with depth (Figure 5b). In 25% of grid boxes, κ_h varied with depth by more than an order of magnitude, primarily at lower latitudes where surface values are elevated. Only 4% of grid boxes had variations with depth that were less than a factor of two. These statistics underestimate the full variability of κ_h since only the upper 1000 to 2000 m is considered.

5. Conclusions

Argo float observations of temperature and salinity provide a near-global estimate of the persistent spatial pattern of salinity variability beneath the ocean's surface. Such salinity anomalies on density surfaces, i.e., the spice field, are an oceanic tracer as well as an important parameter for acoustic propagation in the ocean [e.g., *Dzieciuch et al.*, 2004]. Throughout the ocean, horizontal stirring is more influential than vertical mixing in determining the magnitude of salinity anomalies on density surfaces. The standard deviation of salinity anomalies varies geographically by about two orders of magnitude, with elevated values coincident with enhanced large-scale salinity gradients. The vast majority of inferred mixing lengths (96%) are less than the 600 km gradient scale, consistent with local stirring by eddies. Thus, the advection of salinity anomalies over long distances by closed eddies [e.g., *Armi et al.*, 1988] does not appear to be of leading order importance to the standard deviation of salinity anomalies. Horizontal diffusivity and observed salinity anomalies result from horizontal stirring by eddies of all sizes.

Inferred mixing length and horizontal diffusivity vary with depth and geographic location by more than an order of magnitude. Enhanced values are observed in western boundary current extension regions, the Antarctic Circumpolar Current, and near the equator. Diffusivity had subsurface maxima in 27% of locations and changes with depth that exceeded one order of magnitude in 25% of locations. Equatorial diffusivity, especially at depth, is poorly observed or understood and so deserves additional attention. The diffusivity, estimated here at a 300 km scale, (i) is limited in direction by the use of only a single tracer with large-scale gradients across mean streamlines and (ii) likely has errors due to the use of velocity fluctuations from a state estimate rather than direct measurements, which are not available globally at depth. In addition, regions with potentially large mixing lengths, primarily due to small mean salinity gradients, were excluded from this analysis due to the requirement that mixing-length estimates not exceed 600 km. The agreement in spatial pattern with theoretical predictions supports the conclusion that the Argo-based diffusivity estimate accurately reflects the geographic and depth variability of horizontal diffusivity. The estimated mixing lengths and horizontal diffusivities can be used to test and constrain predictions and parameterizations of eddy stirring.

Argo float observations present a rich and growing data set with which to investigate horizontal stirring and diffusivity. As the number of Argo observations increases, statistics, especially at depths below 1000 m, and the geographic extent, especially in the Southern Ocean, will improve. Temporal changes, on seasonal timescales for example, in stirring and diffusivity can be potentially investigated. Application of this method on a global scale as additional tracers become available (e.g., oxygen) has the potential to refine the estimated horizontal diffusivity.

Acknowledgments
Argo data were collected and made freely available by the international Argo project and the national programs that contribute to it. Argo float data and metadata are from the Global Data Assembly Center (ARGO GDAC; doi: 10.12770/1282383d-9b35-4eaa-a9d6-4b0c24c0cfc9). We are also grateful to the ECCO2 project for making their data freely available via ecco2.jpl.nasa.gov/products. This work was supported by the National Science Foundation under grants OCE-13-55668 and OCE-95-21468 and the Office of Naval Research under grants N00014-12-1-0336 and N00014-13-1-0484.

The Editor thanks Andreas Klocker and an anonymous reviewer for assistance evaluating this paper.

References

Abernathey, R. P., and J. Marshall (2013), Global surface eddy diffusivities derived from satellite altimetry, *J. Geophys. Res. Oceans*, *118*, 901–916, doi:10.1002/jgrc.20066.

Armi, L., and H. Stommel (1983), Four views of a portion of the North Atlantic Subtropical Gyre, *J. Phys. Oceanogr.*, *13*, 828–857.

Armi, L., D. Hebert, N. Oakey, J. Price, P. L. Rishardson, T. Rossby, and B. Ruddick (1988), The history and decay of a Mediterranean salt lens, *Nature*, *333*, 649–651.

Bates, M., R. Tulloch, J. Marshall, and R. Ferrari (2014), Rationalizing the spatial distribution of mesoscale eddy diffusivity in terms of mixing length theory, *J. Phys. Oceanogr.*, *44*, 1523–1540.

Brandt, P., V. Hormann, B. Bourles, J. Fischer, F. A. Schott, L. Stramma, and M. Dengler (2008), Oxygen tongues and zonal currents in the equatorial Atlantic, *J. Geophys. Res.*, *113*, C04012, doi:10.1029/2007JC004435.

Chelton, D. B., R. A. DeSzoeke, and M. G. Schlax (1998), Geographical variability of the first baroclinic Rossby radius of deformation, *J. Phys. Oceanogr.*, *28*, 433–460.

Chelton, D. B., M. G. Schlax, and R. M. Samelson (2011), Global observations of nonlinear mesoscale eddies, *Prog. Oceanogr.*, *91*, 167–216.

Chen, R., J. L. McClean, and S. T. Gille (2014), Isopycnal eddy diffusivities and critical layers in the Kuroshio Extension from an eddying ocean model, *J. Phys. Oceanogr.*, *44*, 2191–2211.

Cole, S. T., and D. L. Rudnick (2012), The spatial distribution and annual cycle of upper ocean thermohaline structure, *J. Geophys. Res.*, *117*, C02027, doi:10.1029/2011JC007033.

Cole, S. T., D. L. Rudnick, and J. A. Colosi (2010), Seasonal evolution of upper-ocean horizontal structure and the remnant mixed layer, *J. Geophys. Res.*, *115*, C04012, doi:10.1029/2009JC005654.

Danabasoglu, G., and J. Marshall (2007), Effects of vertical variations of thickness diffusivity in an ocean general circulation model, *Ocean Modell.*, *18*, 122–141.

Danabasoglu, G., and J. C. McWilliams (1995), Sensitivity of the global ocean circulation to parameterizations of mesoscale tracer transports, *J. Clim.*, *8*, 2967–2987.

Dzieciuch, M., W. Munk, and D. L. Rudnick (2004), Propagation of sound through a spicy ocean, the SOFAR overture, *J. Acoust. Soc. Am.*, *116*, 1447–1462.

Eden, C., M. Jochum, and G. Danabasoglu (2009), Effects of different closures for thickness diffusivity, *Ocean Modell.*, *26*, 47–59.

Ferrari, R., and M. Nikurashin (2010), Suppression of eddy diffusivity across jets in the Southern Ocean, *J. Phys. Oceanogr.*, *40*, 1501–1519.

Ferrari, R., and K. L. Polzin (2005), Finescale structure of the T-S relation in the Eastern North Atlantic, *J. Phys. Oceanogr.*, *35*, 1437–1454.

Ferreira, D., J. Marshall, and P. Heimbach (2005), Estimating eddy stresses by fitting dynamics to observations using a residual-mean ocean circulation model and its adjoint, *J. Phys. Oceanogr.*, *35*, 1891–1910.

Fox-Kemper, B., R. Lumpkin, and F. O. Bryan (2013), Lateral transport in the ocean interior, in *Ocean Circulation and Climate: A 21st Century Perspective*, *Int. Geophys. Ser.*, vol. 103, edited by G. Siedler et al., chap. 8, pp. 185–209, Academic Press, Oxford, U. K.

Funk, A., P. Brandt, and T. Fischer (2009), Eddy diffusivities estimated from observations in the Labrador Sea, *J. Geophys. Res.*, *114*, C04001, doi:10.1029/2008JC005098.

Greatbatch, R. J., P. Brandt, M. Claus, S.-H. Didwischus, and Y. Fu (2012), On the width of the equatorial deep jets, *J. Phys. Oceanogr.*, *42*, 1729–1740.

Griesel, A., S. T. GIlle, J. Sprintall, J. L. McClean, J. H. LaCasce, and M. E. Maltrud (2010), Isopycnal diffusivities in the Antarctic Circumpolar Current inferred from Lagrangian floats in an eddying model, *J. Geophys. Res.*, *115*, C06006, doi:10.1029/2009JC005821.

Holte, J., and L. Talley (2009), A new algorithm for finding mixed layer depths with applications to Argo data and Subantarctic Mode Water formation, *J. Atmos. Oceanic Technol.*, *26*, 1920–1939.

Jenkins, W. J. (1987), 3H and 3He in the Beta Triangle: Observations of gyre ventilation and oxygen utilization rates, *J. Phys. Oceanogr.*, *17*, 763–783.

Johnson, G. C., S. Schmidtko, and J. M. Lyman (2012), Relative contributions of temperature and salinity to seasonal mixed layer density changes and horizontal density gradients, *J. Geophys. Res.*, *117*, C04015, doi:10.1029/2011JC007651.

Klocker, A., and R. Abernathey (2014), Global patterns of mesoscale eddy properties and diffusivities, *J. Phys. Oceanogr.*, *44*, 1030–1046.

Klocker, A., R. Ferrari, and J. H. LaCasce (2012a), Estimating suppression of eddy mixing by mean flows, *J. Phys. Oceanogr.*, *42*, 1566–1576.

Klocker, A., R. Ferrari, J. H. LaCasce, and S. T. Merrifield (2012b), Reconciling float-based and tracer-based estimates of lateral diffusivities, *J. Mar. Res.*, *70*, 569–602.

LaCasce, J. H., R. Ferrari, J. Marshall, R. Tulloch, D. Balwada, and K. Speer (2014), Float-derived isopycnal diffusivities in the DIMES experiment, *J. Phys. Oceanogr.*, *44*, 764–780.

Ledwell, J. R., A. J. Watson, and C. S. Law (1998), Mixing of a tracer in the pycnocline, *J. Geophys. Res.*, *103*, 21,499–21,529, doi:10.1029/98JC01738.

Liu, C., A. Kohl, and D. Stammer (2012), Adjoint-based estimation of eddy-induced tracer mixing parameters in the global ocean, *J. Phys. Oceanogr.*, *42*, 1186–1206.

Marshall, J., A. Adcroft, C. Hill, L. Perelman, and C. Heisey (1997), A finite-volume, incompressible Navier Stokes model for studies of the ocean on parallel computers, *J. Geophys. Res.*, *102*, 5753–5766, doi:10.1029/96JC02775.

Menemenlis, D., I. Fukumori, and T. Lee (2005), Using Green's Functions to calibrate and Ocean General Circulation Model, *Mon. Weather Rev.*, *133*, 1224–1240.

Menemenlis, D., J.-M. Campin, P. Heimbach, C. Hill, T. Lee, A. Nguyen, M. Schodlok, and H. Zhang (2008), ECCO2: High resolution global ocean and sea ice data synthesis, *Mercator Ocean Q. Newsl.*, *31*, 13–21.

Munk, W. (1981), Internal waves and small-scale processes, in *Evolution of Physical Oceanography: Scientific Surveys in Honor of Henry Stommel*, edited by B. A. Warren and C. Wunsch, pp. 264–291, MIT Press, Cambridge, Mass.

Naveira Garabato, A. C. N., R. Ferrari, and K. L. Polzin (2011), Eddy stirring in the Southern Ocean, *J. Geophys. Res.*, *116*, C09019, doi:10.1029/2010JC006818.

Okubo, A. (1971), Oceanic diffusion diagrams, *Deep Sea Res.*, *18*, 789–802.

Prandtl, L. (1925), Bericht untersuchungen zur ausgebildeten turbulenz, *Z. Angew. Math. Mech.*, *5*, 136–139.

Richardson, L. F. (1926), Atmospheric diffusion on a distance-neighbor graph, *Proc. R. Soc. London, Ser. A*, *110*, 707–737.

Roemmich, D., and J. Gilson (2009), The 2004–2008 mean and annual cycle of temperature, salinity, and steric height in the global ocean from the Argo program, *Prog. Oceanogr.*, *82*, 81–100.

Roemmich, D., G. C. Johnson, S. Riser, R. Davis, J. Gilson, W. B. Owens, S. L. Garzoli, C. Schmid, and M. Ignaszewski (2009), The Argo program observing the global ocean with profiling floats, *Oceanography*, *22*(2), 34–43.

Stammer, D. (1998), On eddy characteristics, eddy transports, and mean flow properties, *J. Phys. Oceanogr.*, *28*, 727–739.
Taylor, G. I. (1915), Eddy motion in the atmosphere, *Philos. Trans. R. Soc. London, Ser. A*, *215*, 1–26.
Tennekes, H., and J. L. Lumley (1972), *A First Course in Turbulence*, 300 pp., MIT Press, Cambridge, Mass.
Tulloch, R., J. Marshall, and C. Hill (2011), Scales, growth rates, and spectral fluxes of baroclinic instability in the ocean, *J. Phys. Oceanogr.*, *41*, 1057–1076.
Tulloch, R., R. Ferrari, O. Jahn, A. Klocker, J. LaCasce, J. R. Ledwell, J. Marshall, M.-J. Messias, K. Speer, and A. Watson (2014), Direct estimate of lateral eddy diffusivity upstream of Drake Passage, *J. Phys. Oceanogr.*, *44*, 2593–2616.
Veronis, G. (1972), Properties of seawater defined by temperature, salinity, and pressure, *J. Mar. Res.*, *30*, 227–255.
Vollmer, L., and C. Eden (2013), A global map of meso-scale eddy diffusivities based on linear stability analysis, *Ocean Modell.*, *72*, 198–209.
Waugh, D. W., and E. R. Abraham (2008), Stirring in the global surface ocean, *Geophys. Res. Lett.*, *35*, L20605, doi:10.1029/2008GL035526.
Wortham, C. (2013), A multi-dimensional spectral description of ocean variability with applications, PhD thesis, MIT/WHOI Joint Program, Cambridge, Mass.
Wunsch, C. (1999), Where do ocean eddy heat fluxes matter?, *J. Geophys. Res.*, *104*, 13,235–13,249, doi:10.1029/1999JC900062.
Zhang, H.-M., M. D. Prater, and T. Rossby (2001), Isopycnal Lagrangian statistics from the North Atlantic Current RAFOS float observations, *J. Geophys. Res.*, *106*, 13,817–13,836, doi:10.1029/1999JC000101.
Zhurbas, V., and I. S. Oh (2003), Lateral diffusivity and Lagrangian scales in the Pacific Ocean as derived from drifter data, *J. Geophys. Res.*, *108*(C5), 3141, doi:10.1029/2002JC001596.
Zhurbas, V., and I. S. Oh (2004), Drifter-derived maps of lateral diffusivity in the Pacific and Atlantic Oceans in relation to surface circulation patterns, *J. Geophys. Res.*, *109*, C05015, doi:10.1029/2003JC002241.
Zhurbas, V., D. Lyzhkov, and N. Kuzmina (2014), Drifter-derived estimates of lateral eddy diffusivity in the World Ocean with emphasis on the Indian Ocean and problems of parameterisation, *Deep Sea Res., Part I*, *83*, 1–11.
Zika, J. D., T. J. McDougall, and B. M. Sloyan (2010), Weak mixing in the Eastern North Atlantic: An application of the tracer-contour inverse method, *J. Phys. Oceanogr.*, *40*, 1881–1893.